

From electron tomography of dislocations to field dislocation mechanics: application to olivine

Timmo Weidner¹, Vincent Taupin^{2,3} , Sylvie Demouchy^{4,5} ,
Karine Gouriet¹ , Antoine Guitton^{2,3} , Patrick Cordier^{1,6} 
and Alexandre Mussi^{1,*} 

¹ Univ. Lille, CNRS, INRAE, Centrale Lille, UMR 8207 - UMET - Unité Matériaux et Transformations, Lille F-59000, France

² Université de Lorraine, CNRS, Arts et Métiers, LEM3, Metz 57070, France

³ LabEx DAMAS, Université de Lorraine, Metz 57070, France

⁴ Géosciences Montpellier, Université de Montpellier & CNRS, UMR 5243, F-34095 Montpellier, France

⁵ Laboratoire Magmas et Volcans, Université Clermont Auvergne, CNRS, IRD & OPGC, UMR 6524, F-63170 Aubière, France

⁶ Institut Universitaire de France, F-75005 Paris, France

E-mail: alexandre.mussi@univ-lille.fr

Received 21 July 2023; revised 10 October 2023

Accepted for publication 7 November 2023

Published 24 November 2023



CrossMark

Abstract

We propose a new procedure to extract information from electron tomography and use them as an input in a field dislocation mechanics. Dislocation electron tomography is an experimental technique that provides three-dimensional (3D) information on dislocation lines and Burgers vectors within a thin foil. The characterized 3D dislocation lines are used to construct the spatial distribution of the equivalent Nye dislocation density tensor. The model dislocation lattice incompatibility equation and stress balance equation are solved with a spectral code based on fast Fourier transform algorithms. As an output of the model, one obtains the 3D distribution of mechanical fields, such as strains, rotations, stresses, resolved shear stresses (RSSs) and energy, inside the material. To assess the potential of the method, we consider two regions from a previously compressed olivine sample. Our results reveal significant local variations in

* Author to whom any correspondence should be addressed.



Original content from this work may be used under the terms of the [Creative Commons Attribution 4.0 licence](https://creativecommons.org/licenses/by/4.0/). Any further distribution of this work must maintain attribution to the author(s) and the title of the work, journal citation and DOI.

local stress fields and RSSs in various slip systems, which can impact the strong plastic anisotropy of olivine and the activation of different dislocation slip systems. It also evidences the built-up of kinematic hardening down to the nanometre scale.

Supplementary material for this article is available [online](#)

Keywords: dislocations, electron tomography, mechanics, plasticity, olivine

1. Introduction

Making the link between plastic flow and the dynamics of crystal defects (dislocations) that causes it is a formidable challenge that requires the description of their collective behaviour at the mesoscopic scale [1]. To this end, mesoscopic simulations such as discrete dislocation dynamics (DDD) [2, 3] represent a powerful analysis tool that should be complementary to experimental observations of dislocations. Complementary experimental/modelling analysis of dislocation microstructures can bring valuable insights about elementary deformation mechanisms. Transmission electron microscopy (TEM) is usually the experimental tool of choice for this kind of investigation since it allows a fine characterization of dislocations and their interactions. However, the understanding of the three-dimensional (3D) microstructures is difficult since we only have access to 2D projections and the tilt capabilities are physically limited in microscopes. Dislocation electron tomography (DET) has been developed to overcome these limitations. The basic principle as originally proposed by Barnard *et al* [4] is to perfectly orient the diffraction vector used to image the dislocations parallel to the tilt axis, maintaining at best as possible the Bragg deviation parameter. This technique has been applied in numerous studies as analyses of dislocation microstructures near cracks [5, 6], characterization of helical configurations of dislocations [7–9], analyses of specific interactions of dislocations [10], studies of interactions of dislocations with grain and sub-grain boundaries [11–14], analyses of dislocation microstructures in a carbide [15] and minerals [16–19]. The DET has been the subject of several recent reviews [20–23]. Recent developments include reconstructions from few projected images using black & white contrasts of dislocations [9, 19] or ‘stereo-pair’ method [24–27], machine-learning reconstruction [28] and 4D analysis [9]. In the present contribution, we propose to use electron tomography to get access to the line directions of the dislocation segments. The association of these line directions with their corresponding Burgers vectors allows the construction of the Nye dislocation density tensor at any point in the reconstructed space. Subsequently, the Nye dislocation density tensor leads up to the prediction of the internal mechanical fields (strain, stress, energy, etc.) through the use of a field dislocation mechanics (FDM) model that allows to build a bridge between real dislocation microstructures and continuum mechanics. To illustrate the potential of this DET/FDM analysis method, we consider here as a benchmark the characterization of dislocation networks in an experimentally deformed olivine sample. We will consider in this work two different areas from a deformed single crystal. We reveal for this complex material (limited number of dislocation slip systems, strong plastic anisotropy) a 3D stress state characterized by significant spatial variations and long-range elastic interactions between dislocations. The resulting distribution of dislocation driving stresses allows suggesting possible active slip systems and the strong heterogeneity of distributions shows that the history of dislocation dynamics and the associated build-up of kinematic hardening can be captured with the proposed method.

2. Materials and deformation experiments

This study was carried out on an olivine sample (PoEM9) experimentally deformed by Demouchy *et al* [29] which had already been the focus of TEM microstructural investigations [10, 17]. These axial compression experiments were carried out on a cylinder (length 6.32 mm; diameter 4.19 mm) specimen extracted from a large, gem-quality, single crystal of San Carlos olivine ($(\text{Mg}_{0.91}\text{Fe}_{0.09}\text{Ni}_{0.003})_2\text{SiO}_4$). The sample PoEM9 [29], was deformed along [502] in a high-resolution gas-medium high-pressure apparatus [30] at 806 °C, with a constant strain rate of $5.1 \times 10^{-5} \text{ s}^{-1}$, under a gaseous (Ar) confining pressure of 300 MPa. The finite strain reached was $\varepsilon_{\text{Total}} = 10.1\%$ (obtained post-mortem) and the maximum differential stress was 754 MPa.

3. Methods

3.1. TEM

A complete characterization of the dislocations must include not only the Burgers vectors, but also the geometry of the lines and their habit planes.

3.1.1. Indexation of Burgers vectors. In the early 1980s, Ishida *et al* [31] have shown that the product of the Burgers vectors \mathbf{b} of a dislocation and the diffraction vector \mathbf{g} used to perform the weak-beam dark-field (WBDF) image is equal to the number of thickness fringes which ends at the extremity of this considered dislocation (the direction of the ending thickness fringes is linked to the sign of the Burgers vector [32]).

Figure 1 gives an example of a typical WBDF micrograph of PoEM9 where the diffraction vector $\mathbf{g} : 004$ was used to image dislocations (this reflection was chosen as it has the highest structure factor in olivine). The $\mathbf{g} \cdot \mathbf{b}$ product is equal to ± 4 with a $\pm [001]$ Burgers vector. This number clearly corresponds to the number of terminating thickness fringes seen in figures 1(b) and (c).

Asymmetry of the contrast intensity of dislocation extremities is linked to the sign of the Burgers vectors. This information can be compared to the one obtained from the directions of terminating thickness fringes (figure 2). Taking all these indices into account, we were able to determine most of the Burgers vector signs.

3.1.2. Dislocation geometry characterization. The electron tomography technique entails acquiring a tilt-series and then utilizing a reconstruction algorithm to obtain a corresponding 3D model of the microstructure. As outlined in prior studies [8, 16], the principal impediment to performing electron tomography of dislocations is to maintain a diffraction contrast (which is highly sensitive to the thin foil orientation) constant across the tilt-series. In order to address this issue, the diffraction vector, used to image dislocations, must be precisely aligned with the principal axis of the sample-holder. Furthermore, a slight precession of the electron beam is applied to homogenize the background contrasts (including the presence of thickness fringes) and the dislocation contrasts (oscillating contrasts of dislocations which cross the thin foil thickness) [16, 33]. To enhance the dislocation contrasts, a numerical filter has been employed in ImageJ to adjust the contrast. Reconstructions are then conducted with the weighted back-projection algorithm [34], while dislocations are directly redrawn into the reconstructed volume using markers, facilitated by the Chimera-UCSF software [8, 9, 15, 18–20, 35], to attain precisely the 3D coordinates of the dislocation core images.

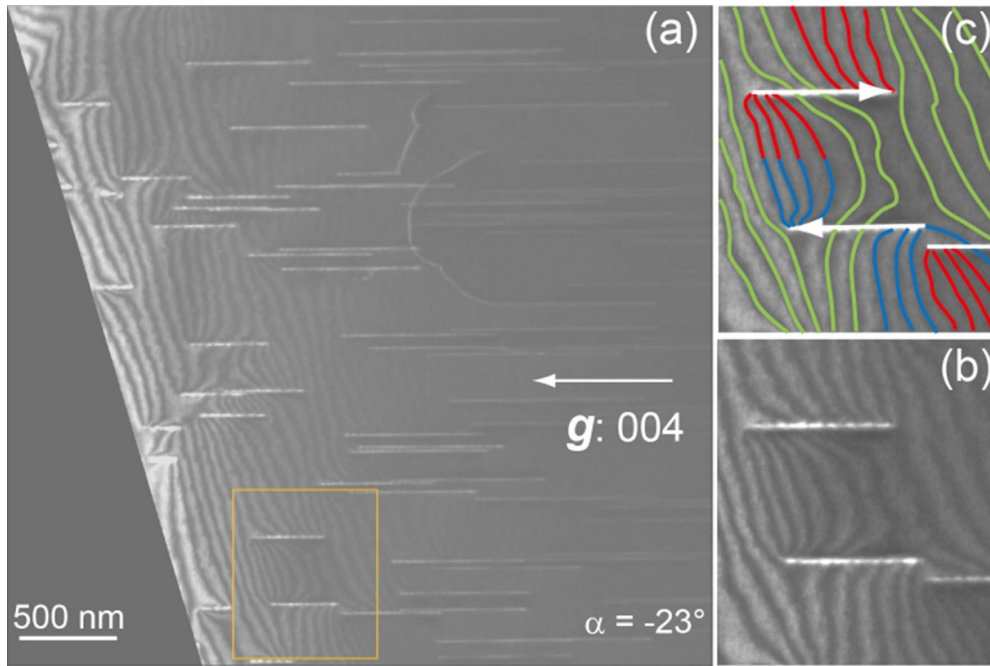


Figure 1. WBDF micrograph obtained with the 004 diffraction vector: (a) global micrograph where thickness fringes are clearly seen; (b) enlargement of a dislocation dipole pointed out by an orange rectangle on figure 1(a); (c) enlargement of the dipole where the un-terminated thickness fringes are coloured in green, the terminated thickness fringes are coloured in red at the extremities of the dislocations represented with arrows oriented on the opposite direction of the wedge, and the terminated thickness fringes are coloured in blue at the extremities of the dislocation represented with an arrow oriented on the direction of the wedge (the directions of the arrows are linked with the signs of the Burgers vectors).

3.2. Nye tensor and elastic field distribution in an anisotropic elastic material

The FDM model employed here [36] introduces discrete dislocation lines, as characterized by tomography, in the form of equivalent continuous dislocation density spatial distributions on a regular 3D grid made of voxels. As an output, the model provides the equilibrated stress field in the voxelized thin foil volume, as well as the associated elastic displacements, strains, and rotations. The characteristics of dislocations, namely their line directions and their Burgers vectors, are introduced through the Nye dislocation tensor in the model [37]. The Nye tensor α is a second-order tensor with components $\alpha_{ij} = B_i t_j$ in the Cartesian coordinate system ($\mathbf{e}_1, \mathbf{e}_2, \mathbf{e}_3$) aligned with the thin foil frame. The quantity B_i is a length of Burgers vector per unit surface and can be written $B_i = nb/\Delta_S \mathbf{e}_i$, where n is the number (not necessarily an integer) of dislocations of Burgers vector magnitude b along the direction \mathbf{e}_i , and Δ_S is the spatial resolution surface. The vector \mathbf{t} is the local dislocation line unit vector. For instance, an edge (respectively screw) dislocation with line along the \mathbf{e}_3 direction and with Burgers vector along the \mathbf{e}_1 (respectively \mathbf{e}_3) direction corresponds to an edge (respectively screw) dislocation density α_{13} (respectively α_{33}). A mixed dislocation would be made of both densities. In practice, any 3D dislocation line or segment can be transferred into an equivalent Nye dislocation density distribution in a volume. In the case of a regular grid made of voxels to be used later for fast

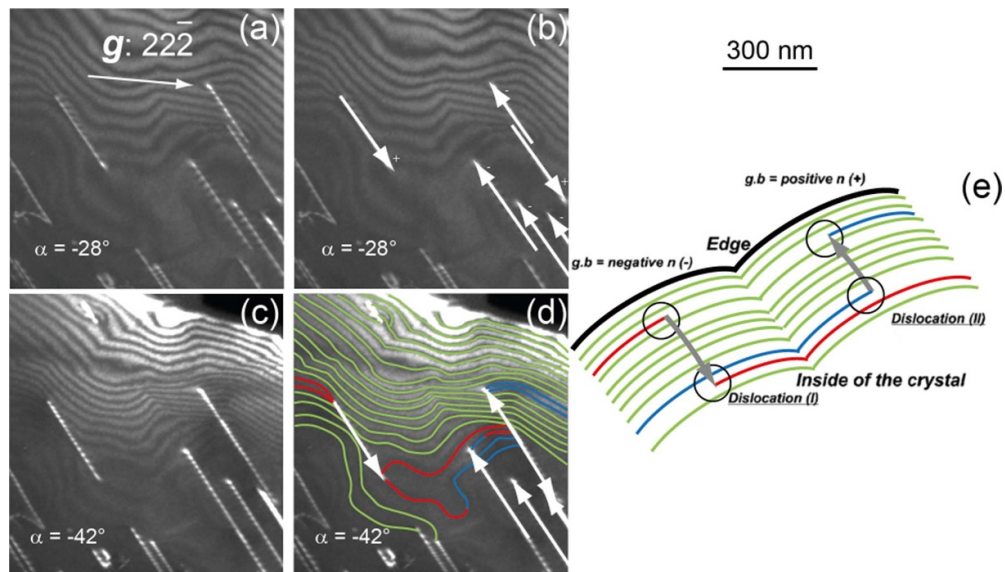


Figure 2. Association of the intensity of the dislocation extremities with the sign of the Burgers vector: (a) Raw micrograph in WBDF conditions, obtained with the 222 diffraction vector (with a projection angle of -28°), where an intensity asymmetry of dislocation extremities is clearly seen; (b) arrows added on the raw micrograph of figure 2(a) = the arrow is oriented in the direction of the intense extremity of the dislocation; (c) raw micrograph of the same domain with a projection angle of -42° ; (d) arrows and thickness fringes added and redrawn on the raw micrograph of figure 2(c) where the thickness fringes are coloured in green when they are not terminated on the extremities of dislocations, in red at the extremities of the dislocations represented with arrows oriented on the opposite direction of the wedge, and in blue at the extremities of the dislocation represented with an arrow oriented on the direction of the wedge; (e) cartoon extracted from Miyajima and Walte [32], where the method to get access to the $\mathbf{g} \cdot \mathbf{b}$ product is described, taking into account the signs of the Burgers vectors, following Ishida *et al* [31], with the same colour code and arrow direction code as figure 2(d). A link between the intensity of the dislocation extremities and the sign of the Burgers vector is noticeably evident. Reprinted from [32], Copyright (2009), with permission from Elsevier.

Fourier transform (FFT) based numerical calculation of elastic fields, we use the recent method proposed by Bertin [38] to transform discrete dislocation segments into equivalent dislocation densities properly assigned on voxels. Note that a similar approach was also proposed very recently [39]. The method used is briefly presented below, the reader is referred to [38] for more details.

Figure 3 illustrates a part of a discrete dislocation line composed of three straight segments shown in red in the figure. The figure shows a two-dimensional setup for clarity, but the calculation is performed in three dimensions. The second (middle) dislocation segment is considered here and shown as a bold red line. It is defined by its starting point, \mathbf{x}_a , and its ending point, \mathbf{x}_b , following the direction of the segment line vector \mathbf{t} . The thin dashed black lines delimit the grid voxels used in the numerical algorithm used to solve FDM equations. The voxel size is H_1 , H_2 , and H_3 in the \mathbf{x}_1 , \mathbf{x}_2 , and \mathbf{x}_3 directions. The position of the centre of voxel d considered in the figure is given by its position vector \mathbf{x}_d . Its volume is denoted $\Omega_d = H_1 \times H_2 \times H_3 = H^3$ where we chose that $H_1 = H_2 = H_3 = H$. For the voxel d , a surrounding box of dimension

The integral $I(\mathbf{x}_d)$ can be numerically evaluated as

$$I(\mathbf{x}_d) = (s^b - s^a) - A_1 - A_2 - A_3 + B_{12} + B_{13} + B_{23} - C_{123}, \quad (3)$$

with the terms

$$\left\{ \begin{array}{l} A_i = \frac{1}{H_i} \left[d_i s - \frac{1}{2} t_i s^2 \right]_a^b, \\ B_{ij} = \frac{1}{H_i H_j} \left[d_i d_j s - \frac{1}{2} (d_i t_j + t_i d_j) s^2 + \frac{1}{3} t_i t_j s^3 \right]_a^b, \\ C_{ijk} = \frac{1}{H_i H_j H_k} \left[d_i d_j d_k s - \frac{1}{2} (t_i d_j d_k + d_i t_j d_k + d_i d_j t_k) s^2 \right. \\ \left. + \frac{1}{3} (d_i t_j t_k + t_i d_j t_k + t_i t_j d_k) s^3 - \frac{1}{4} t_i t_j t_k s^4 \right]_a^b. \end{array} \right. \quad (4)$$

The domain $[s_a, s_b]$ is divided into portions $[a, b]$ on which the sign of $\prod_i^n (d_i - s t_i)$ does not change. For each voxel d , the dislocation density is the sum of all densities due to all dislocation segments that cross the surrounding box shown in figure 3. The process is repeated for all voxels forming the simulation volume. Given an initial Nye dislocation density in a volume, we are now interested in numerically estimating the associated internal stress field within a small strain anisotropic elasticity mechanical framework. We rely on the FDM model [36]. We denote by \mathbf{U}_e the elastic distortion of a 3D body containing dislocations. In the absence of dislocations, the distortion would be the gradient of the elastic displacement vector \mathbf{u}_e , that is $\mathbf{U}_e = \mathbf{grad}(\mathbf{u}_e)$. However, it is not true anymore in the presence of dislocations due to discontinuities in the elastic displacement field, i.e. the Burgers vectors of dislocations. As such, the elastic distortion must contain an incompatible, non-gradient, curl part ($\mathbf{curl}(\chi)$), which is related to the Nye tensor. The elastic distortion is thus written as

$$\mathbf{U}_e = \mathbf{U}_e^{\parallel} + \mathbf{U}_e^{\perp} = \mathbf{grad}(\mathbf{u}_e) + \mathbf{curl}(\chi). \quad (5)$$

The elastic distortion resumes to the compatible, gradient part, in the absence of dislocations, while the incompatible, curl part, is related to the Nye tensor through the incompatibility equation

$$\mathbf{curl}(\mathbf{U}_e^{\perp}) = \alpha = \mathbf{curl}(\mathbf{curl}(\chi)), \quad (6)$$

where the curl operator removes the compatible part of the elastic distortion. For a given distribution of Nye dislocation density in a volume, the elastic incompatible distortion is obtained from the solution of equation (6). Then, the compatible elastic distortion is generally nonzero and ensures the balance of stresses inside the volume. That writes

$$\mathbf{div}(\sigma) = \mathbf{div}(\mathbf{C} : \mathbf{U}_e) = \mathbf{div}(\mathbf{C} : (\mathbf{U}_e^{\parallel} + \mathbf{U}_e^{\perp})) = \mathbf{0} \quad (7)$$

where σ is the Cauchy stress tensor and \mathbf{C} is the fourth-order elastic moduli tensor. The above equation can be rearranged as

$$\mathbf{div}(\mathbf{C} : \mathbf{grad}(\mathbf{u}_e)) = -\mathbf{div}(\mathbf{C} : (\mathbf{U}_e^{\perp})), \quad (8)$$

and solved for the elastic displacement field \mathbf{u}_e . Once the elastic displacement is known, the compatible elastic distortion is obtained from its gradient and the total elastic distortion is finally obtained by adding the incompatible part. The total, balanced, stress field σ is then obtained by multiplication by the elastic stiffness tensor \mathbf{C} . Solving equations (6)–(8) for a given distribution of Nye tensor provides a unique solution for the associated internal stress field [40]. Numerical solutions can be obtained from finite element approximations [41] and

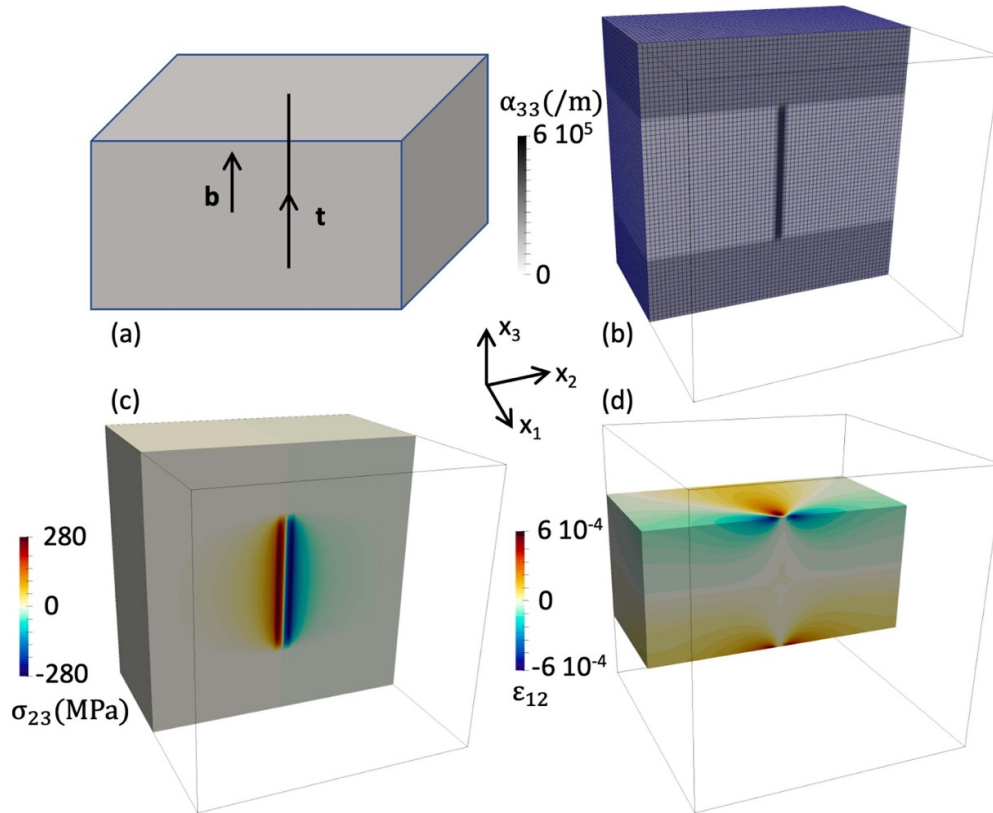


Figure 4. Numerical strategy to model the stress field of discrete dislocation lines observed by tomography in a thin foil. (a) Sketch of a thin foil containing one vertical threading screw dislocation line (black solid line, the line and Burgers vectors are also indicated). (b) Corresponding Nye tensor screw component α_{33} on the 3D FFT grid (clip). Bright voxels belong to the thin foil while dark voxels correspond to the gas phase. (c) Internal shear stress field σ_{23} . (d) Elastic strain field ε_{12} generated near and at the free surfaces of the thin foil to cancel the internal stresses σ_{13} and σ_{23} at the free surfaces. The coordinate system used for figures (b), (c), (d) is shown at the centre of the figure.

from spectral methods [42]. The latter rely on the use of FFT algorithms [43] and allow simulations of large 3D volumes. Here, we employ an FFT spectral approximation, based on the accelerated scheme [44] and using a special treatment for the evaluation of the modified Green tensor in the Fourier space [45]. The reader is referred to [42] for details, whereby a very similar spectral algorithm was developed. We now describe the FFT simulation setup to model the dislocations observed in a thin foil by tomography and obtain their internal stress/strain fields. Figure 4 illustrates the main steps. We consider as an illustrative example a foil of dimension $960 \text{ nm} \times 960 \text{ nm}$ with a thickness of 480 nm shown in figure 4(a). A vertical screw dislocation line which crosses perpendicularly the two surfaces of the foil (threading dislocation) is inserted in the middle of the foil and shown by the solid black line. The FFT grid is here a cube made of $64 \times 64 \times 64$ voxels. The voxel size, i.e. the spatial resolution of FDM, is set to 15 nm in all simulations. Figure 4(b) shows the associated Nye tensor component α_{33} distributed on the FFT grid after the ‘Nye’zation’ procedure described above. Note that all

dislocation densities are embedded inside the FFT volume. To create the two external free surfaces of the thin foils, where the stress field must satisfy zero-traction boundary conditions, we use a so-called gas phase, which is common in FFT simulations. Voxels with much lower elastic stiffness compose the gas phase. The interfaces between material voxels (with normal stiffness) and gas phase voxels are free surfaces, where the stress field satisfies zero-traction boundary conditions. An example of this gas phase method can be found in [42], where the stress field of an edge dislocation line near a pore was simulated and found to agree quantitatively very well with the existing analytical solution. In figure 4(b), one can see how the external free surfaces of the foil are created in the present FDM FFT simulation. Bright voxels compose the foil material, while dark voxels compose the so-called gas phase. More precisely, the elastic stiffness tensor \mathbf{C} of the olivine material will be attributed to each bright voxel, while a much lower stiffness (10^4 times smaller) is attributed to the dark voxels. In doing so, the internal stresses will be affected near the two free surfaces to satisfy zero-traction boundary conditions. Figure 4(c) shows the internal shear stress field σ_{23} due to the dislocation line in the foil, obtained after convergence of the FDM-FFT numerical algorithm. One can see that it is affected by the external surfaces and tends to zero at them. Figure 4(d) also shows the elastic strain ε_{12} generated near and at the free surfaces to cancel the internal stresses σ_{13} and σ_{23} . A qualitative agreement is observed with elastic fields due to a threading screw dislocation in GaN, simulated by FDM with a finite element approximation [41]. Note finally that because the Nye dislocation density is numerically spread on FFT voxels, dislocation lines have an apparent core in the FDM simulations, with a size the order of the FFT voxel length (15 nm), but it is to be interpreted as a numerical core, rather than a physical core. Note that the FDM can be applied to model dislocation cores [46], but it is not the scope of the present work. The spatial resolution is here 15 nm, much too large to properly describe real dislocation cores. The consequence of having numerical dislocation cores is that the internal stresses are smoothed and not well captured near the physical dislocation cores, but far from the dislocation cores (a few nm) it is correctly rendered. Short-term stress core corrections can be added [38, 39] and are important when dealing with small scale DDD, dislocation line tension effects and dislocation reactions. In the present work however, it is not critical and does not alter our findings, as we consider mostly straight dislocation lines separated by distances much larger than the physical core size of dislocations. Furthermore, the resolution (15 nm) is already small such that large stresses between dislocation lines can already be predicted (see next section).

4. Results and discussion

4.1. Dislocation microstructure

In order to take an overall look at the PoEM9 microstructure of dislocations, six tilt-series (obtained with the $22\bar{2}$ diffraction vector) were acquired at a low magnification, which represents an analysed total area of approximately $30 \mu\text{m}^2$ [17], with an average angular range from -52° to 48° .

Burgers vector indexations are performed using the thickness fringes technique [31] with the 004 and $22\bar{2}$ diffraction vectors (figures 1 and 2 respectively). They showed that the microstructures are only composed of dislocations with [001] Burgers vectors and overwhelmingly with straight screw dislocation characters. An example of dislocation microstructure obtained in WBDF conditions with the 004 diffraction vector is shown in figure 1. The electron tomography shows a majority of $\{110\}$ and (100) glide planes, few cross-slip configurations [17] and colinear interactions [17]. The reconstructed volumes also provide access to (\mathbf{u}, \mathbf{b}) doublets

for each dislocation segment, to calculate the Nye tensor, and to simulate the continuous distribution of stress field.

Two domains of specimen PoEM9 are studied in detail: zone 1 on figures 5(a)–(d) and zone 2 on figures 5(e)–(h). A tilt-series composed of 51 micrographs (acquired every 2° with a tilt angle ranging from -48° to $+52^\circ$) and a second tilt-series of 54 micrographs (acquired every 2° with a tilt angle ranging from -56° to $+50^\circ$) were obtained in WBDF conditions with the $22\bar{2}$ diffraction vector (zones 1 and 2 respectively). Micrographs from figures 5(a) and (e) come from these two tilt-series for a projection angle of 0° . Electron tomography reconstructions enable the characterization of the (110), $(1\bar{1}0)$ and (100) slip systems which are identified by their colours: white, light grey and black respectively as in Mussi *et al* [17]. Neither the slip systems of the pure screw straight dislocations (coral pink-coloured), nor the habit plane of the red sessile dislocation segment in figure 5(f), can be indexed. Then, the reconstructed volumes are projected along the [001] direction in order to orientate the pure screw dislocations in edge-on position (figures 5(c) and (g)) and thereafter, to provide optimal viewing conditions to study the continuous stress distributions.

4.2. Simulation results

The dislocation internal stresses in the thin foil are rotated in the olivine crystal reference frame. The x_1 , x_2 and x_3 directions are now aligned with the a , b and c directions of the olivine orthorhombic unit cell, respectively. In addition to this internal stress, we add the macroscopic stress applied experimentally during the compression test (754 MPa) and also rotated in the crystal reference frame. This is possible since we know the angle between the normal of the thin foil $[17\bar{5}12]$ and the compression axis $[502]$ (approximately 30°). The total stress field at every voxel in the thin foil is then $\sigma_{ij} = \sigma_{ij}^{\text{int}} + \Sigma_{ij}$, where σ_{ij}^{int} is the local internal stress field due to dislocations and Σ_{ij} is the macroscopic stress. It is then possible to project the total stress tensor at every voxel on different slip systems using the associated Schmid tensor expressed in the olivine orthorhombic reference frame. In the following, we consider three slip systems, labelled 1, 2 and 3: $[001](100)$, $[001](110)$ and $[001](1\bar{1}0)$ respectively. The resolved shear stress (RSS) for the three systems are denoted by RSS1, RSS2 and RSS3 in the following. They are equal to:

$$\begin{aligned} \text{RSS1} &= \tau^{[001](100)} = \sigma_{31}, \\ \text{RSS2} &= \tau^{[001](110)} = \frac{b}{\sqrt{a^2 + b^2}} \sigma_{31} + \frac{a}{\sqrt{a^2 + b^2}} \sigma_{32} \approx 90.63\% \sigma_{31} + 42.26\% \sigma_{32}, \\ \text{RSS3} &= \tau^{[001](1\bar{1}0)} = \frac{b}{\sqrt{a^2 + b^2}} \sigma_{31} - \frac{a}{\sqrt{a^2 + b^2}} \sigma_{32} \approx 90.63\% \sigma_{31} - 42.26\% \sigma_{32}. \end{aligned} \quad (9)$$

with a and b the directions of the olivine orthorhombic unit cell.

The macroscopic stress $\Sigma_{31} = 10ac\sigma / [(5a)^2 + (2c)^2] \approx 302.8$ MPa (with a and c the directions of the olivine orthorhombic unit cell and σ the applied stress) while $\Sigma_{32} = 0$. Figures 5 and 6 show the spatial distribution of the three RSSs on slices in the thin foil, for the two thin foil series. Dislocation lines are shown in figure 5. They are removed in figure 6 for a better comparison of RSS distributions in different slip systems. RSS1, RSS2 and RSS3 fields look similar, local rotations of RSS patterns (lobes) near dislocations can be seen between the three RSS maps. The distribution of the internal elastic energy density $1/2 \varepsilon_{ij}^e C_{ijkl} \varepsilon_{kl}^e$ is also shown in figure 6. It shows elastic interactions between dislocations (interacting elastic fields between dislocations). Note that the calculation of the mean internal elastic energy within the thin foil volume give 51.6 kJ m^{-3} for series 1 and 52.2 kJ m^{-3} for series 5. The reader is

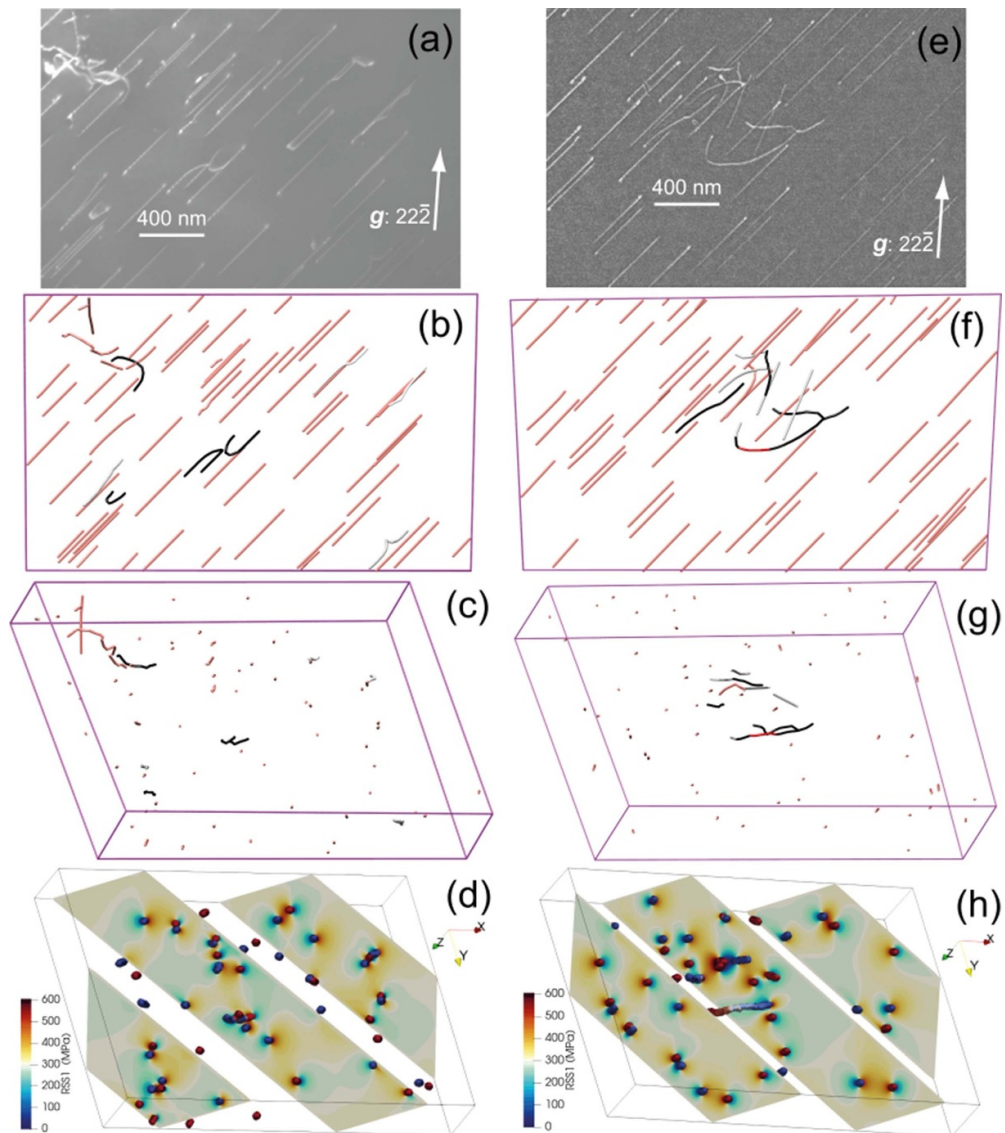


Figure 5. Link between TED and FDM: (a) raw micrograph in WBDF conditions, obtained with the $22\bar{2}$ diffraction vector (with a projection angle of 0°) of zone 1; (b) reconstructed volume of the same domain with the same projected angle (the (110) , $(\bar{1}\bar{1}0)$ and (100) slip systems are respectively coloured in white, light grey and black as in [17]); (c) reconstructed volume of the same domain along the $[001]$ direction; (d) spatial distributions (3 slices) of RSS1 in series 1 obtained along the same orientation as figure 5(c) located in the interaction between the two black dislocations in the middle of the micrograph in figures 5(a) and (b) (dislocation lines are also shown and coloured w.r.t. their sign.); (e) raw micrograph in WBDF conditions, obtained with the $22\bar{2}$ diffraction vector (with a projection angle of 0°) of zone 2; (f) reconstructed volume of the same domain with the same projected angle (the $(\bar{1}\bar{1}0)$ and (100) slip systems are respectively coloured in light grey and black); (g) reconstructed volume of the same domain along the $[001]$ direction; (h) spatial distributions (3 slices) of RSS1 in series 5 obtained along the same orientation as figure 5(g) located in the red dislocation segment (dislocation lines are also shown and coloured with reference to their sign).

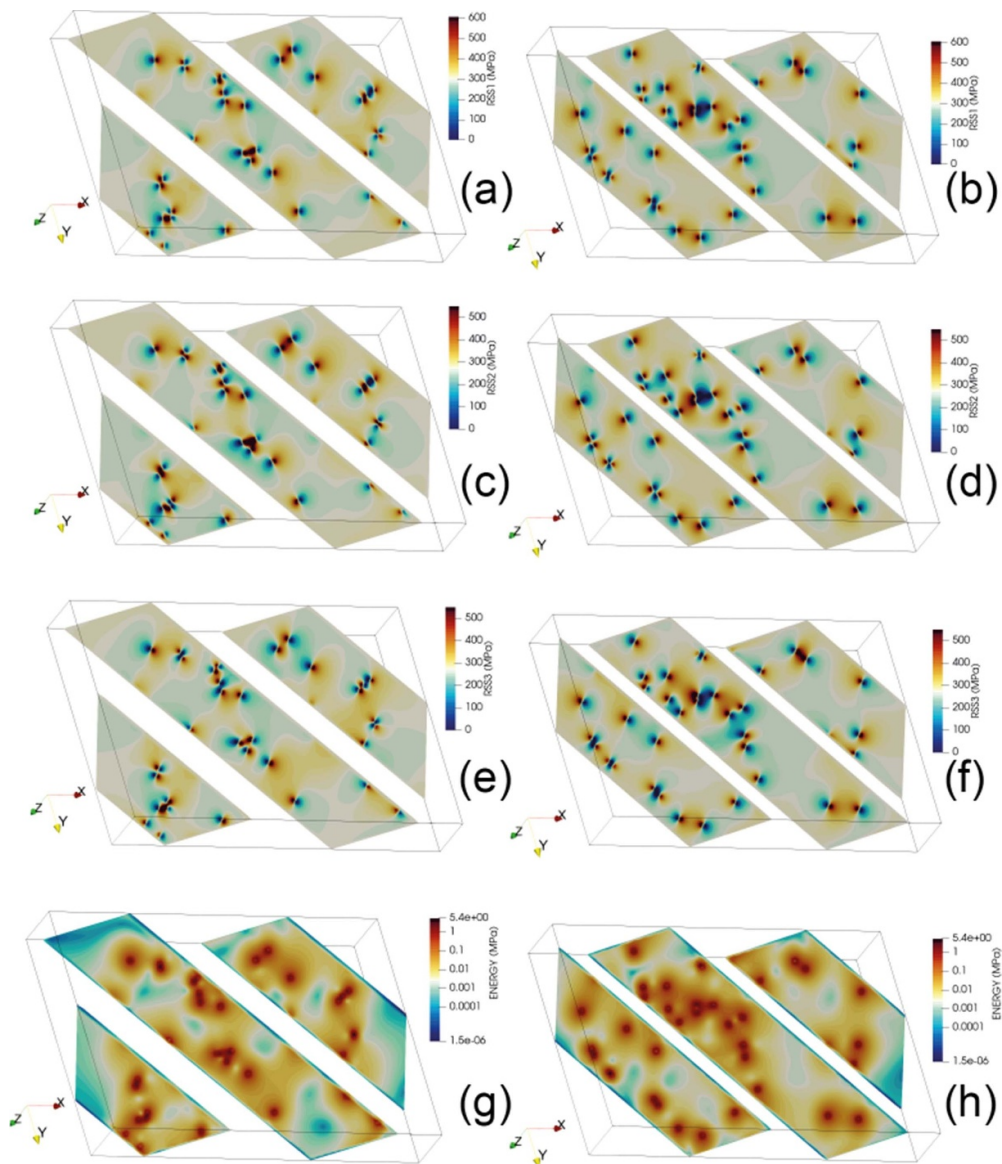


Figure 6. Spatial distributions (3 slices) of RSS1 (a), (b), RSS2 (c), (d), RSS3 (e), (f) and elastic energy density (g), (h) for series 1 (left column) and series 5 (right column).

further referred to animations in the supplementary materials, where moving slices parallel to slip planes allow for a better visualization of the long-range elastic interactions between dislocation lines within the thin foils. Histograms of the RSS distributions in the thin foils are provided in figures 7(a) and (b) showing a significant heterogeneity of the stress field within the thin foils. One can note that the mean value of RSS1 (302.8 MPa) is slightly larger than that of RSS2 and RSS3 (274.4 MPa). This is because the sample was oriented to activate system 1 preferentially. Strong variations in the stress values can be seen, typically ± 400 MPa

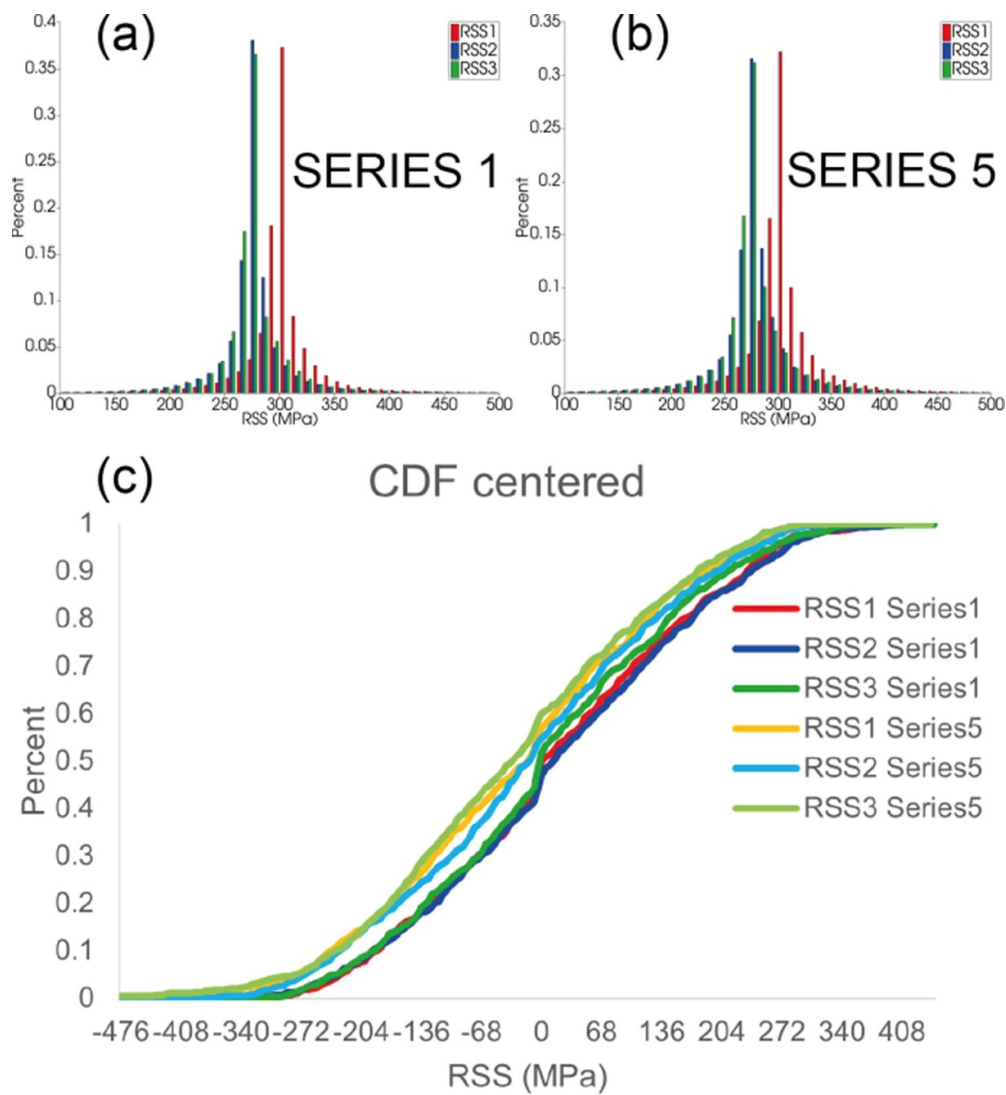


Figure 7. Distributions of RSS1, RSS2 and RSS3 for series 1 (zone 1) and series 5 (zone 2). (a), (b): All RSS values in the thin foils are used. (c): Only RSS values at dislocation lines are used. All cumulative distribution functions (CDF) for the three slip systems and the two series are superimposed on the same figure.

around the mean values. Regions with local stresses reaching 1 GPa are also observed, particularly nearby dislocation dipoles. Finally, figure 7(c) shows cumulative distribution functions (CDFs) for RSS1, RSS2, RSS3, for the two thin foil series, with RSS values extracted only at the dislocation lines (instead of taking values at all voxels in the thin foils). In doing so, we only consider dislocation driving stresses in the single crystal. The CDF are centred about zero. Broad distributions, with again variations up to ± 400 MPa, are clearly evidenced in the CDF for the three slip systems and the two thin foils, and they look rather similar. One clear feature in all these maps and distributions is thus the presence of long-range elastic interactions

between dislocations and significant local variations of the RSS values in the three systems considered due to the complexity of the 3D stress state.

4.3. Discussion

The present coupled electron tomography/FDM analysis allows obtaining for the first time a detailed, 3D, physical/mechanical description of dislocation networks in the studied thin foils. A physical description of dislocations (Burgers vectors, 3D arrangement of dislocation lines, junctions, dipoles, networks) is complemented by a mechanical description (strains, rotations, stresses, energy). In the present study, we specifically discuss two points, (1) the possible activation of different slip systems in olivine deformed at low temperature due to the complexity of the 3D stress state, and (2), the history of dislocation dynamics and the associated build-up of polarized internal stresses and kinematic hardening in single crystals at the nanometre scale.

- (1) Activation of slip systems: The POEM-9 specimen, from which thin foils have been extracted and analysed here, was compressed along the $[502]$ direction, to preferentially activate the $[001](100)$ slip system (system 1 and RSS1). However, an uncertainty between the possible activated slip systems was mentioned [29]. Another system, $[001](110)$ was also proposed as a possible system. A third system could also be activated, $[001](\bar{1}\bar{1}0)$. They correspond to system 2 and system 3 in the present study. Our distributions of RSS values in the thin foil indeed suggest that system 1 is only slightly favoured as compared to systems 2 and 3, because the mean value of RSS1 is only slightly larger (difference of less than 30 MPa). However, in a recent work [17], systems 2 and 3 are observed to be easier to activate (lower CRSS) than system 1, system 1 being the second easiest system to activate after system 2 and 3. As such it is not easy to say which one of system 1 or systems (2, 3) was preferentially activated in our studied sample. The distributions of the RSS values extracted only at dislocation lines are certainly more speaking. Indeed, the distributions show very similar features for all series and slip systems. More precisely, they are all broad and show significant local variations, ± 400 MPa. As such, the slight difference of the mean RSS between system 1 and systems (2, 3), less than 30 MPa, becomes negligible as compared to possible large local values of RSS. From this, we can conclude that, although POEM-9 was compressed in a way to favour slip system 1, the three systems can all be activated, because of the strong heterogeneity of the internal stress field.
- (2) Internal stresses and kinematic hardening: The simulated fields of RSS show a significant heterogeneity. Recently, an experimental work on deformed olivine single crystals and polycrystals using high-resolution-EBSD (HR-EBSD) revealed a pronounced heterogeneity in the in-plane elastic shear strains and shear stresses at the surface [47, 48]. Variations up to ± 1 GPa around the mean value were reported in both polycrystals and single crystals (at low temperatures) at the micron scale. Such polarization and patterning of internal, intragranular and intergranular stresses, can be related to the build-up of geometrically necessary dislocation densities. Strong heterogeneity of internal stresses is to be associated with kinematic hardening. In the present study, we can look at the heterogeneity of internal stresses down to the scale of typical HR-EBSD map pixels, *i.e.* at the nanometre scale. Our results also reveal a significant heterogeneity of internal stresses at the nanometre scale in a single crystal containing dislocation networks. Distributions of RSS show broad profiles, with variations up to ± 400 MPa around the mean value. Interestingly, the histograms show a few negative RSS values. The results thus suggest that kinematic hardening has been built-up and is a signature of the past dynamics of dislocations observed.

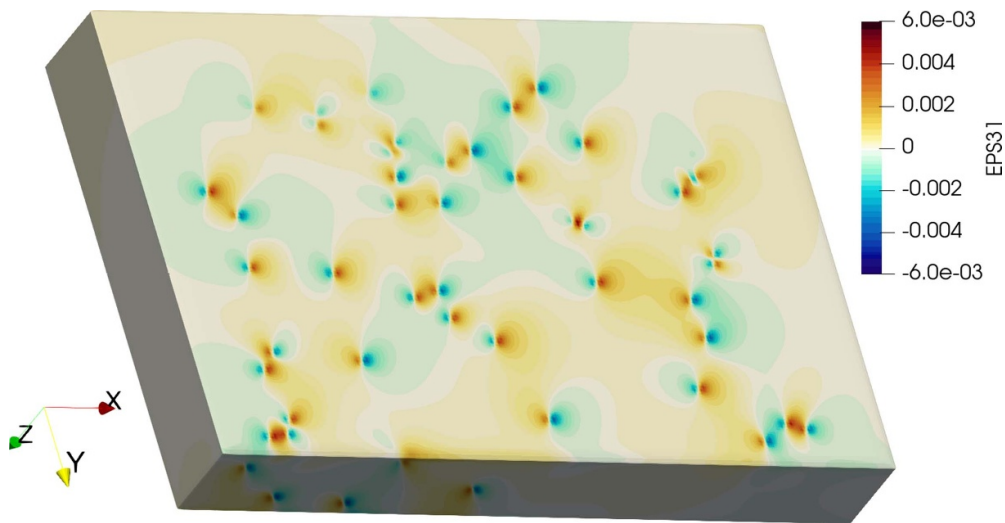


Figure 8. Elastic strain ε_{31} at the surface of the thin foil for series 1.

The application of our electron tomography/FDM method brings valuable insights regarding the complexity of plastic flow in olivine. In a simple single crystal subjected to simple compression loading, it shows that plastic anisotropy and activation of dislocation slip systems can be significantly altered by the large fluctuations of the local mechanical fields. Furthermore, it evidences the built-up of kinematic hardening. This plastic behaviour observed at the single crystal, nanometre scale, certainly has a strong impact on the rheology of olivine polycrystals within the Earth's mantle. More generally, our proposed analysis method can also be employed to investigate other mechanisms and defects typically investigated in the TEM for various crystals, such as subgrain boundaries, dislocation networks, dislocation grain boundary interactions, dislocation reactions, interactions between dislocations and pores/precipitates etc. Furthermore, as shown in figure 8, the method also provides elastic fields in the vicinity of and at free surfaces, which allows making links between elastic fields measurements using experimental techniques such as precession electron diffraction [49], HR-EBSD (high-resolution electron backscatter diffraction), HR-TKD (high-resolution transmission Kikuchi diffraction) [41], ACOM (automated crystal orientation mapping) ASTAR® [50] and defects inside the material. It must be emphasized that, in addition to provide 3D anisotropic elastic fields, our approach allows a spatial resolution of 15 nm in routine use, extendable down to 5 nm. The method can also be used to assess the accuracy of HR-TKD, or ACOM/ASTAR methods, when measuring the elastic fields around dislocation structures.

5. Conclusion

In this contribution, we propose an original experimental and theoretical characterization method for studying dislocation networks in crystalline materials. The method combines DET, which provides a 3D characterization of dislocation lines and Burgers vectors, to a FDM model, which provides the associated internal mechanical fields. To demonstrate the potential of our method, we have considered single crystal thin foils extracted from a compressed olivine single crystal. Our results have revealed significant local fluctuations in the local mechanical fields, particularly the RSSs in different slip systems, which certainly play a role in the

strong anisotropy of olivine and the activation of different dislocation slip systems. Our first results have also evidenced the built-up of kinematic hardening at the nanometre scale in a single crystal. Our method has a considerable potential for studying various types of dislocation microstructures and plastic deformation mechanisms in different crystals.

Data availability statement

The data that support the findings of this study are openly available at the following URL/DOI: <https://doi.org/10.5281/zenodo.8171066>.

Acknowledgments

This project has received funding from the European Research Council (ERC) under the European Union's Horizon 2020 research and innovation program under Grant Agreement No. 787198—TimeMan. A M, V T and A G would like to acknowledge support from the French national research agency (ANR) through the Grant ANR-PRC-2022-MAMIE-NOVA (ANR-22-CE08-0018). The TEM national facility in Lille (France) is supported by the Conseil Regional du Nord-Pas de Calais, the European Regional Development Fund (ERDF), and the Institut National des Sciences de l'Univers (INSU, CNRS).

ORCID iDs

Vincent Taupin  <https://orcid.org/0000-0002-2469-0179>
Sylvie Demouchy  <https://orcid.org/0000-0001-5023-4655>
Karine Gouriet  <https://orcid.org/0000-0003-3148-8849>
Antoine Guitton  <https://orcid.org/0000-0002-1508-787X>
Patrick Cordier  <https://orcid.org/0000-0002-1883-2994>
Alexandre Mussi  <https://orcid.org/0000-0003-2093-0144>

References

- [1] Kubin L P 2013 *Dislocations, Mesoscale Simulations and Plastic Flow (Oxford Series on Materials Modelling)* (Oxford Academic) (<https://doi.org/10.1093/acprof:oso/9780198525011.001.0001>)
- [2] Devincere B and Kubin L P 1997 The modelling of dislocation dynamics: elastic behaviour versus core properties *Phil. Trans. R. Soc. A* **355** 2003–12
- [3] Devincere B, Kubin L P and Hoc T 2006 Physical analyses of crystal plasticity by DD simulations *Scr. Mater.* **54** 741–6
- [4] Barnard J S, Sharp J, Tong J R and Midgley P A 2006a High-resolution three-dimensional imaging of dislocations *Science* **313** 319
- [5] Sharp J H, Barnard J S, Kaneko K, Higashida K and Midgley P A 2008 Dislocation tomography made easy: a reconstruction from ADF STEM images obtained using automated image shift correction *J. Phys.: Conf. Ser.* **126** 1–4
- [6] Tanaka M, Higashida K, Kaneko K, Hata S and Mitsuhashi M 2008 Crack tip dislocations revealed by electron tomography in silicon single crystal *Scr. Mater.* **59** 901–4
- [7] Feng Z Q, Lin C W, Li T T, Luo X, Wu G L and Huang X X 2017 Electron tomography of dislocations in an Al-Cu-Mg alloy *IOP Conf. Ser.: Mater. Sci. Eng.* **219** 012018
- [8] Mussi A, Addad A and Onimus F 2021a Dislocation electron tomography: a technique to characterize the dislocation microstructure evolution in zirconium alloys under irradiation *Acta Mater.* **213**
- [9] Mussi A, Carrez P, Gouriet K, Hue B and Cordier P 2021b 4D electron tomography of dislocations undergoing electron irradiation *C. R. Phys.* **22** 67–81

- [10] Mussi A, Cordier P and Demouchy S 2015a Characterization of dislocation interactions in olivine using electron tomography *Phil. Mag.* **95** 335–45
- [11] Kacher J P, Liu G S and Robertson I M 2011 Visualization of grain boundary/dislocation interactions using tomographic reconstructions *Scr. Mater.* **64** 677–80
- [12] Kacher J and Robertson I M 2012 Quasi-four-dimensional analysis of dislocation interactions with grain boundaries in 304 stainless steel *Acta Mater.* **60** 6657–72
- [13] Kacher J and Robertson I M 2014 In situ and tomographic analysis of dislocation/grain boundary interactions in α -titanium *Phil. Mag.* **94** 814–29
- [14] Chen S and Yu Q 2019 The role of low angle grain boundary in deformation of titanium and its size effect *Scr. Mater.* **163** 148–51
- [15] Mussi A, Cordier P, Ghosh S, Garvik N, Nzogang B C, Carrez P and Garruchet S 2016 Transmission electron microscopy of dislocations in cementite deformed at high pressure and high temperature *Phil. Mag.* **96** 1773–89
- [16] Mussi A, Cordier P, Demouchy S and Vanmansart C 2014 Characterization of the glide planes of the [001] screw dislocations in olivine using electron tomography *Phys. Chem. Miner.* **41** 537–45
- [17] Mussi A, Nafi M, Demouchy S and Cordier P 2015b On the deformation mechanism of olivine single crystals at lithospheric temperatures: an electron tomography study *Eur. J. Miner.* **27** 707–15
- [18] Mussi A, Cordier P, Demouchy S and Hue B 2017 Hardening mechanisms in olivine single crystal deformed at 1090 °C: an electron tomography study *Phil. Mag.* **97** 3172–85
- [19] Mussi A, Gallet J, Castelnau O and Cordier P 2021c Application of electron tomography of dislocations in beam-sensitive quartz to the determination of strain components *Tectonophysics* **803** 228754
- [20] Liu G S, House S D, Kacher J, Tanaka M, Higashida K and Robertson I M 2014 Electron tomography of dislocation structures *Mater. Charact.* **87** 1–11
- [21] Feng Z, Fu R, Lin C, Wu G, Huang T, Zhang L and Huang X 2020 TEM-based dislocation tomography: challenges and opportunities *Curr. Opin. Solid State Mater. Sci.* **24** 1–9
- [22] Hata S et al 2020a Electron tomography imaging methods with diffraction contrast for materials research *Microscopy* **69** 141–55
- [23] Hata S, Honda T, Saito H, Mitsuhashi M, Petersen T C and Murayama M 2020b Electron tomography: an imaging method for materials deformation dynamics *Curr. Opin. Solid State Mater. Sci.* **24** 1–12
- [24] Eftink B P, Gray G T and Maloy S A 2017 Stereographic methods for 3D characterization of dislocations *Microsc. Microanal.* **23** 210–1
- [25] Jácome L A, Pöthkow K, Paetsch O and Hege H-C 2018 Three-dimensional reconstruction and quantification of dislocation substructures from transmission electron microscopy stereo pairs *Ultramicroscopy* **195** 157–70
- [26] Oveisi E, Letouzey A, Alexander D T L, Jeangros Q, Schäublin R, Lucas G, Fua P and Hébert C 2017 Tilt-less 3D electron imaging and reconstruction of complex curvilinear structures *Sci. Rep.* **7** 10630
- [27] Oveisi E, Letouzey A, Zanet S D, Lucas G, Cantoni M, Fua P and Hébert C 2018 Stereo-vision three-dimensional reconstruction of curvilinear structures imaged with a TEM *Ultramicroscopy* **184** 116–24
- [28] Altingövdé O, Mishchuk A, Ganeeva G, Oveisi E, Hebert C and Fua P 2022 3D reconstruction of curvilinear structures with stereomatching deep convolutional neural networks *Ultramicroscopy* **234** 113460
- [29] Demouchy S, Tommasi A, Boffa Ballaran T and Cordier P 2013 Low strength of Earth's uppermost mantle inferred from tri-axial deformation experiments on olivine crystals *Phys. Earth Planet. Int.* **220** 37–49
- [30] Paterson M S 1990 Rock deformation experimentation *The Brittle-Ductile Transition in Rocks: The Head Volume (Geophysical Monograph Series)* ed A Duba et al (AGU) pp 187–94
- [31] Ishida Y, Ishida H, Kohra K and Ichinose H 1980 Determination of the Burgers vector of a dislocation by weak-beam imaging in a HVEM *Phil. Mag. A* **42** 453–62
- [32] Miyajima N and Walte N 2009 Burgers Vector determination in deformed perovskite and post-perovskite of CaIrO₃ using thickness fringes in weak-beam dark-field images *Ultramicroscopy* **109** 683–92

- [33] Rebled J M, Yedra L, Estrade S, Portillo J and Peiro F 2011 A new approach for 3D reconstruction from bright field TEM imaging: beam precession assisted electron tomography *Ultramicroscopy* **111** 1504–11
- [34] Herman G T, Lakshminarayanan A V and Naparstek A 1976 Convolution reconstruction techniques for divergent beams *Comput. Biol. Med.* **6** 259–71
- [35] Pettersen E F, Goddard T D, Huang C C, Couch G S, Greenblatt D M, Meng E C and Ferrin T E 2004 UCSF Chimera: a visualization system for exploratory research and analysis *J. Comput. Chem.* **25** 1605–12
- [36] Acharya A 2001 A model of crystal plasticity based on the theory of continuously distributed dislocations *J. Mech. Phys. Solids* **49** 761–84
- [37] Nye J F 1953 Some geometrical relations in dislocated crystals *Acta Metall.* **1** 153–62
- [38] Bertin N 2019 Connecting discrete and continuum dislocation mechanics: a non-singular spectral framework *Int. J. Plast.* **122** 268–84
- [39] Kohnert A A and Capolungo L 2021 Spectral discrete dislocation dynamics with anisotropic short range interactions *Comput. Mater. Sci.* **189** 110243
- [40] Arora R, Zhang X and Acharya A 2020 Finite element approximation of finite deformation dislocation mechanics *Comput. Methods Appl. Mech. Eng.* **367** 113076
- [41] Ernould C, Taupin V, Beausir B, Fundenberger J J, Maloufi N, Guyon J and Bouzy E 2022 Characterization of a nanopipe dislocation in GaN by means of HR-EBSD and field dislocation mechanics analysis *Mater. Charact.* **194** 112351
- [42] Djaka K S, Villani A, Taupin V, Capolungo L and Berbenni S 2017 Field dislocation mechanics for heterogeneous elastic materials: a numerical spectral approach *Comput. Methods Appl. Mech. Eng.* **315** 921–42
- [43] Frigo M and Johnson S G 2005 The design and implementation of FFTW3 *Proc. IEEE* **93** 216–31
- [44] Michel J C, Moulinec H and Suquet P 2001 A computational scheme for linear and non-linear composites with arbitrary phase contrast *Int. J. Numer. Methods Eng.* **52** 139–60
- [45] Willot F 2015 Fourier-based schemes for computing the mechanical response of composites with accurate local fields *C. R. Mec.* **343** 232–45
- [46] Zhang X, Acharya A, Walkington N J and Bielak J 2015 A single theory for some quasi-static, supersonic, atomic, and tectonic scale applications of dislocations *J. Mech. Phys. Solids* **84** 145–95
- [47] Wallis D *et al* 2020 Dislocation interactions during low-temperature plasticity of olivine and their impact on the evolution of lithospheric strength *Earth Planet. Sci. Lett.* **543** 116349
- [48] Wallis D, Hansen L N, Wilkinson A J and Lebensohn R A 2021 Dislocation interactions in olivine control postseismic creep of the upper mantle *Nat. Commun.* **12** 3496
- [49] Cooper D, Bernier N and Rouvière J L 2015 Combining 2 nm spatial resolution and 0.02% precision for deformation mapping of semiconductor specimens in a transmission electron microscope by precession electron diffraction *Nano Lett.* **15** 5289–94
- [50] Després A and Veron M 2023 Elastic strain field measurements in the TEM for metallurgical applications *Mater. Charact.* **202** 113012